5-20-2015

Epitaxial CrN Thin Films with High Thermoelectric Figure of Merit

Eric L. Thies
Boise State University

Daniel A. Hillsberry
Boise State University

Dmitri A. Tenne
Boise State University

Epitaxial CrN Thin Films with High Thermoelectric Figure of Merit

Camilo X. Quintela
Department of Materials Science and Engineering
University of Wisconsin-Madison
Madison, WI

Dmitri A. Tenne
Department of Physics
Boise State University
Boise, ID

Jacob P. Podkaminer
Department of Materials Science and Engineering
University of Wisconsin-Madison
Madison, WI

Evgeny Y. Tsymbal
Department of Physics and Astronomy
University of Nebraska-Lincoln
Lincoln, NE

Maria N. Luckyanova
Department of Mechanical Engineering
Massachusetts Institute of Technology
Cambridge, MA

Gang Chen
Department of Mechanical Engineering
Massachusetts Institute of Technology
Cambridge, MA

Tula R. Paudel
Department of Physics and Astronomy
University of Nebraska-Lincoln
Lincoln, NE

Chang-Beom Eom*
Department of Materials Science and Engineering
University of Wisconsin-Madison
Madison, WI
eom@engr.wisc.edu

Eric L. Thies
Department of Physics
Boise State University
Boise, ID

and

Daniel A. Hillsberry
Department of Physics
Boise State University
Boise, ID

Francisco Rivadulla*
Centro de Investigación en Química Biológica y
Materiales Moleculares (CIQUS)
University of Santiago de Compostela
Santiago de Compostela, Spain
f.rivadulla@usc.es

Abstract

A large enhancement of the thermoelectric figure of merit is reported in single crystalline films of CrN. The strong reduction of the lattice thermal conductivity in the rock-salt phase of this material is shown to be related to intrinsic lattice instabilities, which is similar to the resonant bonding effect proposed for cubic IV-VI compounds. These results demonstrate that useful ideas from classic thermoelectrics and phase change materials can be extended to transition metal nitrides and oxides.

Keywords: CrN, thin films, thermoelectrics, thermal conductivity, lattice instabilities

The design of efficient thermoelectric (TE) devices for energy harvesting and advanced cooling applications is one of the current challenges in materials science.[1] So far, the most common materials used in commercial TE devices are rock-salt IV-VI (PbTe, PbSe) and distorted rock-salt V_2-VI_3 (Bi_2Te_3, Bi_2Se_3) semiconductors.[2] One of the key factors behind the high TE performance of these materials is their abnormally low lattice thermal conductivity (κ_l), which is one of the fundamental parameters that define the dimensionless TE figure of merit $zT = S^2\sigma T/(\kappa_l+\kappa_e)$, in which S is the Seebeck coefficient, σ the electrical conductivity, T the absolute temperature, and κ_e the electronic thermal conductivity.

In a recent paper, Lee et al.[3] suggested that the main reason for the low lattice thermal conductivity in rock-salt IV-VI compounds is the *resonant bonding* (RB) effect: the *p*-orbitals with 3 electrons per atom cannot form the six saturated bonds of the rock-salt lattice, and therefore an RB structure is established.[4] Using first-principles calculations, they demonstrated that the large electronic polarizability of the resonant bonds introduces long-range interactions and a softening of the transverse optical phonon mode. This ultimately causes acoustic phonon scattering and is responsible for the low lattice thermal conductivity in IV-VI and V_2-VI_3 compounds. An interesting question is whether or not the concept of RB can be extrapolated to transition-metal (TM) compounds with a rock-salt structure. The versatility of the oxidation states and ionic sizes shown by TM ions would offer enormous possibilities for tuning their TE properties, which would allow for new approaches regarding the design of TE materials with improved capabilities.

In this communication we demonstrate that rock-salt CrN shows intrinsic lattice instabilities that suppress its thermal conductivity. Using *ab-initio* calculations, we determined that the origin of these instabilities is similar to that observed in IV-VI compounds with RB states.[3,5] Through the fabrication of high quality epitaxial (001) CrN thin films we report a ≈250% increase in the zT at room temperature compared to bulk CrN.[6] These results along with its high thermal stability, resistance to corrosion, and exceptional mechanical properties, make CrN a promising *n*-type material for high-temperature TE applications.

The presence of extrinsic factors, such as N-vacancies or epitaxial constrains, are likely behind the large variety of structural and transport properties previously reported for CrN films.[7] In the case of polycrystalline bulk CrN, the intergrain contribution to the electrical and thermal conductivities can be significant enough to mask its intrinsic transport properties and, ultimately, its thermoelectric performance. Therefore, in order to access the intrinsic thermoelectric properties of CrN, it is necessary to develop the fabrication of epitaxial, stoichiometric, and fully relaxed CrN films. The results discussed in this paper are based on 68 nm thick (001) CrN films epitaxially grown onto (001) MgO substrates by reactive magnetron sputtering. Those films were post-annealed in ammonia (NH_3) gas at 800ºC for 2h. The temperature and annealing time were carefully optimized in order to achieve the correct stoichiometry (details related to the sample fabrication and characterization are provided in the Experimental Section).

The structural, microstructural, and compositional characterizations of both *as-grown* and *annealed* films are summarized in **Figure 1**. The results demonstrate the high crystalline quality of the CrN films as well as the correct stoichiometry (Cr/N ≈ 1) for the annealed samples, which are fully strain relaxed (bulk-like). Figure 1a displays a θ - 2θ x-ray diffraction (XRD) scan over a 2θ angular range of $42^\circ - 45^\circ$. The plot shows the CrN (002) and MgO (002) reflections for both as-grown and annealed samples, confirming the out-of-plane epitaxy of the films. The absence of thickness fringes in the annealed sample is related to the decrease of the surface smoothness after the annealing, which shows a root mean square roughness R_q= 2.5 nm, four times larger than the as-grown (R_q = 0.6 nm). The in-plane epitaxial relationship between the MgO substrate and the CrN films was determined by off-axis azimuthal ϕ-scans over the (022) peak. A representative ϕ-scan for the annealed sample is shown in Figure 1b. For both as-grown and annealed samples, the scans yielded sharp peaks that were 90° apart at identical azimuthal angles as the substrate, confirming cube-on-cube epitaxial growth [100] CrN // [100] MgO. The evaluation of the in-plane $\Delta\phi$ full width at half maximum (FWHM) revealed a slight improvement of the in-plane crystalline orientation after the annealing, obtaining $\Delta\phi$ = 0.8 for the annealed sample and $\Delta\phi$ = 1.1 for the as-grown. These results are consistent with the reciprocal space mapping (RSM) measurements taken around the CrN (113) lattice point, as shown in Figure 1c. The RSM shows a contour broadening decrease in the in-plane (*HH0*) direction after the annealing, indicating an improvement in the in-plane crystalline quality. In addition, the post-annealing treatment shifts the CrN (113) peak toward the theoretical CrN bulk value, demonstrating that the thermal annealing drives the sample to a completely relaxed (bulk-like) lattice.

The microstructural and chemical composition of the samples were determined by cross-sectional scanning transmission electron microscopy (STEM) and electron energy loss spectroscopy (EELS). Measurements of the relative Cr and N intensities of the EEL spectra, shown in Figure 1d, revealed a Cr excess in the as-grown sample. In contrast, a Cr/N ratio of almost unity was observed in the annealed sample, demonstrating that post-deposition annealing in NH_3 is necessary to obtain stoichiometric CrN films. The thickness of the samples, measured directly from the TEM images, was found to be 68 ± 0.2 nm, value consistent with the values derived from the x-ray reflectivity analysis. The impact of the annealing treatment in the film's microstructure was further investigated through high-

resolution STEM. Figure 1e displays the interface between CrN and MgO with a high-resolution STEM image for CrN in the inset, in which a high degree of crystallinity can be observed. These results demonstrate that the annealing treatment improves the stoichiometry of the sample without a deterioration in the crystallinity.

An additional characteristic feature of stoichiometric CrN is the presence of a structural phase transition at T_N = 286 K from a high temperature rock-salt structure (space group *Fm3n*) to a low temperature orthorhombic phase (space group *Pnma*).[8] This structural transition is known to be sensitive to the presence of N vacancies [9] and also to the epitaxial strain induced by the substrate.[7] In order to identify the structural transition in the annealed sample, Raman spectra were acquired at different temperatures. As shown in **Figure 2**, the change of modes with temperature confirms the structural phase transition in this sample (details about the mode's assignments are provided in the Supporting Information). From the temperature dependence of the 7 THz mode, the structural phase transition temperature was estimated to occur at ~ 287 K, as reported for stoichiometric CrN.[8,9] Therefore, the confirmation of the structural transition at ~ 287 K in the annealed CrN films, along with the high crystalline quality and correct stoichiometric composition obtained from XRD and EELS experiments, indicates that the measured transport properties in the annealed samples are intrinsic to CrN.".

The representative thermoelectric properties for the annealed sample in comparison with the as-grown are shown in **Figure 3**. The temperature dependence of the thermal conductivity, which is dominated by the lattice thermal conductivity,[10] is presented in Figure 3a. The as-grown sample shows low κ, which decreases monotonically with temperature. These features are characteristic of glasses or materials with point defects that act as scatter centres for phonons, so we attribute this behaviour to the presence of N-vacancies in the as-grown film. On the other hand, two clear trends that are linked to the crystal structure of the film can be distinguished in the annealed sample: In the low temperature orthorhombic phase, the larger value of κ and its temperature dependence are the expected behaviour for crystalline materials, with the characteristic phonon peak maxima observed around 250 K. At the structural phase transition, κ abruptly drops and becomes almost temperature independent in the high temperature rock-salt phase. This type of dependence has previously reported for stoichiometric bulk CrN[5] and suggests the presence of an intrinsic (structural dependent) mechanism of phonon scattering in rock-salt CrN (RS-CrN), which is suppressed in the orthorhombic phase.

The presence of intrinsic lattice instabilities in RS-CrN can be understood using a simple model based on chemical bonding. In binary TM nitrides, three of the five *d*-orbitals of the metal hybridize with the three $2p^3$-orbitals of N to form a band of bonding and antibonding states (BS and ABS, respectively) separated by an energy gap. The remaining two *d*-orbitals do not participate in the bond and form a band of non-bonding states (NBS), which have energy close to that of the atomic *3d*-orbitals. In the case of ScN, the three valence electrons of Sc ([Ar] $4s^2\ 3d^1$) and the three *p*-electrons of N will completely fill the BS, forming a semiconducting perfectly stable rock-salt structure, as observed experimentally in oxygen-free films.[11] Introducing further electrons (Ti, V, etc.) will start filling the NBS, giving rise to the metallic conductivity observed in these compounds. This situation should continue until MnN, when the band of NBS is completely full. Adding more electrons beyond this point will begin the populating of the ABS, destabilizing the rock-salt structure. In fact, FeN and CoN show a fourfold coordination (zincblende structure).[12] Taking these considerations into account, CrN should be located very close to the stability limit of the rock-salt structure for TM mononitrides with the Fermi level (E_F) located in a sharp band with a 3*d* character formed by the NBS. Although this is a simplified description of a more complex band structure [13], it captures the main contributions to the chemical bond in CrN, and it was a useful guide to identify CrN as a potential system with strong lattice instabilities that suppress the thermal conductivity.

In order to test the previous hypothesis and to investigate the correlation between the low thermal conductivity observed in RS-CrN and its structural stability, we performed first-principles calculations in a supercell approach as implemented in Phonopy [14] with the atomic force calculated using VASP.[15] **Figure 4** shows the calculated volume dependence of the TO mode frequency at the zone center for rock-salt (*Fm3m*) and orthorhombic (*Pnma*) CrN. These results are compared with neighboring binary nitrides (TiN and ScN) that show a stable rock-salt structure. The results for RS-CrN were found to be dependent on the magnetic structure of the material (the phonon band spectra for different phases is provided in Supporting Information). The TO phonon in non-magnetic (NM) RS-CrN is anomalously softer than that of ScN and TiN, compounds that show larger thermal conductivities than CrN.[16] Furthermore, while the frequency of the TO mode depends linearly on the volume for the ScN and TiN the dependence is quadratic in NM RS-CrN, which indicates the strong anharmonicity of this mode. As a result, the calculated Gruneisen parameter (γ) of rock-salt CrN is much larger than that of ScN and TiN (Supporting Information). Conversely, the TO phonons in

orthorhombic (*Pnma*) CrN are quasi-harmonic, and the Gruneisen parameter is smaller, which is similar to the behavior observed in cubic ScN and TiN. All of these results point to the presence of intrinsic lattice instabilities in RS-CrN, which explains the low thermal conductivity in this phase.

On the basis of the simplified band structure previously discussed for CrN, conducting electrons in a narrow band of NBS are expected to produce a large Seebeck coefficient in this materials that increases linearly with temperature according to the Mott formula for degenerate semiconductors. [17] This hypothesis is consistent with the experimental data in which a large $|S|$, that linearly increases with temperature was observed in the *annealed* sample (Figure 3b). The lower $|S|$ measured in the as-grown sample could be related to N vacancies: since CrN is an *n*-type material, further electron doping would lead to a reduction of the absolute value of the Seebeck coefficient. Although both the temperature dependence and the absolute value of the Seebeck coefficient for the annealed sample are consistent with previously reported results for stoichiometric bulk CrN,[6] the measured resistivity is much lower (Figure 3c). Given that the electronic carrier concentration in the annealed sample (n = 5.6 – 6.8 x 10^{19} cm^{-3}) is similar to that observed in stoichiometric bulk CrN, [6] this reduction of the resistivity is due to an increased electron mobility resulting from the improved crystalline quality in the films (The mobility measured at 350 K in the annealed CrN film, μ_H = 125 $cm^2V^{-1}s^{-1}$, is almost 100 times larger than the value observed in bulk CrN at the same temperature, μ_H = 1.5 $cm^2V^{-1}s^{-1}$). The presence of a sharp jump in the resistivity at ~ 287 K, as observed in stoichiometric bulk CrN [6, 18] additionally confirms the correct stoichiometry and homogeneity in the annealed sample. Conversely, the as-grown films show a broad-transition, semiconducting-like behavior in the whole temperature range, and larger resistivity due to a decrease in electron mobility. The obtained value at room temperature, μ_H = 1.18 $cm^2V^{-1}s^{-1}$, is about 110 times smaller than the value obtained for the annealed sample). These results confirm that the electron transport in CrN is strongly dependent on the N-vacancy concentration, which may cause carrier localization, as previously reported. [19]

The low electrical resistivity observed in the annealed sample along with its large $|S|$ lead to a remarkably high power factor that reaches $PF \approx 15$ μW $cm^{-1}K^{-2}$ at 300 K. This value is nearly five times larger than the reported value for optimized bulk CrN at the same temperature [6] and comparable to the high temperature value observed in ScN[16, 20] and other commercial thermoelectric materials, such as B-doped SiGe ($PF \approx 19$ μW $cm^{-1}K^{-2}$),[21] and $La_3Te_{4-x}Pb_x$, ($PF \approx 14$ μW $cm^{-1}K^{-2}$ at 1100 K).[22] The combination of this large PF and the intrinsically low thermal conductivity in RS-CrN results in a high zT = 0.12 at room temperature for the annealed sample (Figure 3d), which is a value similar to that shown in other state-of-the-art thermoelectric materials at the same temperature.[23] This high zT in the annealed sample means more than a 250% enhancement compared with the optimized bulk material.[6]

In summary, we report on the fabrication and the thermoelectric characterization of stoichiometric and high-quality epitaxial CrN (001) films with large zT. Based on theoretical calculations, we demonstrate that the anomalously low thermal conductivity observed in rock-salt CrN is due to intrinsic lattice instabilities, whose origin is very similar to that of IV-VI alloys with resonant bonding. The extension of this principle to transition metal compounds (nitrides, oxides, etc.) would open new avenues toward the design of new materials with optimized TE and phase change properties. From an experimental point of view, we first show that the post-annealing of epitaxial CrN thin films in an NH_3 atmosphere leads to an improvement of the stoichiometry, which provides access to the intrinsic thermoelectric properties of this material. The combination of a high power factor in the annealed samples and the intrinsically low thermal conductivity of rock-salt CrN results in a high zT of ~ 0.12 at room temperature, which increases very rapidly with increased in temperature without signs of saturation. The possibility of doping the material with other transition metals or the fabrication of multilayers offers multiple possibilities to further improve the thermoelectric performance of CrN. These results, along with its high thermal and chemical stability and exceptional mechanical properties, make CrN a promising *n*-type material for high temperature thermoelectric power generation.

Experimental Section

Sample Fabrication: CrN thin films were deposited by DC reactive planar magnetron sputtering onto (001) MgO single crystal substrates at 500 °C in an Ar (20 sccm)/N_2 (4 sccm) atmosphere at 7.4 mTorr. A 99.99% pure 2 in. Cr target was sputtered at 146 W in DC constant power mode. After the deposition, the samples were cooled-down in vacuum and post-annealed in a tube furnace in ammonia (NH_3) gas for 2 hours at 800 °C to improve the Cr/N stoichiometry.

Structural Characterization: The structural and microstructural properties of the films were characterized using four-circle x-ray diffraction (XRD) and scanning transmission electron microscopy (STEM). The STEM was performed at the Advanced Microscopy Laboratory (Zaragoza, Spain) in a FEI Titan 60-300 operated at 300 kV. Z contrast imaging was carried out in a High Angle Annular Dark Field (HAADF) with a probe convergence angle of 25 mrad and an inner collection angle of approximately 58 mrad. The HAADF imaging was combined with Electron Energy Loss Spectroscopy (EELS) to chemically analyze the heterostructures by Spectrum Imaging (SI).

Raman Measurements: The Raman spectra was measured in backscattering geometry normal to the film surface using a Jobin Yvon T64000 triple spectrometer. An ultraviolet excitation (325 nm line of He-Cd laser) was used for excitation. The maximum laser power density was 0.5 W mm^{-2} at the sample surface, which was low enough to avoid any noticeable local heating of the sample.

Thermoelectric Characterization: The temperature dependent resistivity, Hall Effect, and Seebeck coefficient measurements were all performed inside a continuous flow cryostat under a dynamic vacuum ($\sim 10^{-5}$ mbar). Resistivity and Hall measurements were performed in CrN thin films patterned into a Hall bar geometry. The Seebeck coefficient was measured in a custommade device with spring-loaded copper fins providing electrical and thermal contact on the films subjected to a stabilized temperature gradient. Data were determined as the linear relationship between the induced voltages and the temperature differences. Both GaAs thermometers and Chromel-Constantan thermocouples were used to sense the temperature gradient, yielding consistent and reproducible results.

Time Domain Thermoreflectance: Time domain thermoreflectance (TDTR) was used to measure the thermal conductivity of the CrN films. A 100 nm opto-thermal Al transducer layer was deposited on the sample by e-beam evaporation. In the experiment, a strong laser pulse impinges on the opto-thermal transducer where the light is absorbed and converted into a heat pulse, which propagates through the sample. A time-delayed probe pulse measures the changing reflectivity of the surface of the sample, which can then be directly related to the changing temperature of the sample. The resulting cooling curve was fit with a least-squares minimization technique to the solution of the Fourier heat conduction equation applied to a multi-dimensional, multi-layer stack to determine the unknown properties. The multi-layer stack consisted of an Al opto-thermal transducer layer, the interface between the Al and the CrN film underneath, the CrN film, and finally the MgO substrate, which was treated as semiinfinite. The thermal transport properties of the MgO substrate used herein were separately measured by TDTR and used as a parameter in the fitting. The interface conductance between the Al and the CrN was allowed to float, as was the thermal conductivity of the CrN itself. The experimental system used herein has been elaborated on elsewhere.[24] Although the thermal conductivity was measured in a direction perpendicular to the film plane, we assumed that the thermal conductivity was isotropic for the zT calculation, which is a reasonable assumption given the RS structure of CrN.

Phonon Band Structure Calculations: Phonon band structure and mode Gruneisen parameters were calculated using the supercell approach as implemented in Phonopy with a 2 x 2 x 3 supercell for the orthorhombic phase (96 atoms) and a 2 x 2 x 2 supercell of a conventional cell (64 atoms) for the rock salt phase. The atomic forces were calculated by VASP using the Hellmann Feynman Theorem and a kinetic energy cutoff of 500 eV. The correlation effects were treated at the GGA+U level with a U=3.0 eV. The obtained band structure were verified against that calculated using a large supercells calculation and a frequency at the center of the Brillouin zone with those calculated in a density functional perturbation theory (DFPT)[25] as implemented in VASP.

Supporting Information

Supporting Information is available from the Wiley Online Library or from the author.

Acknowledgements

This work was supported by the ERC (ERC-StGrant 2DTHERMS) and the National Science Foundation (NSF) under DMREF Grant No. DMR-1234096. Work at MIT on TDTR is funded by 'Solid State Solar-Thermal Energy Conversion Center (S^3TEC)', an Energy Frontier Research Center funded by the US Department of Energy, Office of Science, and Office of Basic Energy Sciences under Award Number: DE-SC0001299/DE-FG02-09ER46577. Raman studies at Boise State University were supported by NSF under grant DMR-1006136, and M. J. Murdock Charitable Trust "Partners in Science" program. F. R. acknowledges financial support from MINECO-Spain (MAT2013-44673-R), Xunta de Galicia (2012-CP071).

References

[1] F. J. Di Salvo, *Science* **1999**, *285*, 703; L. E. Bell, *Science* **2008**, *321*, 1457.

[2] G. J. Snyder, E. S. Toberer, *Nat. Mater.* **2008**, *7*, 105; J. P. Heremans, M. S, Dresselhaus, L. E. Bell, D. T Morelli, *Nat. Nanotechnol.* **2013**, *8*, 471.

[3] S. Lee, K. Esfarjani, T. Luo, J. Zhou, Z. Tian, G. Chen, *Nat. Comm*. **2014,** *5*, 4525.

[4] G. Lucovsky. R. M. White, *Phys. Rev. B*. **1973**, *8*, 660.

[5] K. Shportko, S. Kremers, M. Woda, D. Lencer, J. Robertson, M. Wutting, *Nature Mater*. **2008,** *7*, 653; D. Lencer, M. Salinga, B. Grabowski, T. Hickel, J. Neugebauer, M. Wutting, *Nature Mater*. **2008,** *7*, 972.

[6] C. X. Quintela, F. Rivadulla, J. Rivas, *Appl. Phys. Lett.* **2009**, *94*, 152103; C. X. Quintela, F. Rivadulla, J. Rivas, *Phys, Rev. B*. **2010**, *82*, 245201; C. X. Quintela, B. Rodriguez-Gonzalez, F. Rivadulla, *Appl. Phys. Lett.* **2014**, *104*, 022103.

[7] D. Gall, C.-S. Shin, r. T. Haasch, I. Petrov, J. E. Greene, *J. Appl. Phys*. **2002**, *91*, 5882; A. Ney, R. Rajaram, S. S. P. Parkin, T. Kammermeier, S. Dhar, *Appl. Phys. Lett*. **2006,** *89*, 112504; K. Inumaru, K. Koyama, N. Imo-oka, S. Yamanaka, *Phys. Rev. B*. **2007**, *75*, 054416; X. Y. Zhang, J. S. Chawla, R. P. Deng, D. Gall, *Phys. Rev. B*. **2011**, *84*, 073101; X. F. Duan, W. B. Mi, Z. B. Guo, H. L. Bai. *J. Appl. Phys*. **2013**, *113*, 023701.

[8] L. M. Corliss, N. Elliott, J. M. Hastings, *Phys. Rev.* **1960**, *117*, 926.

[9] J. D. Browne, P. R. Liddell, R. Street, T. Mills, *Phys. Status Solidi A*. **1970**, *1*, 715. [10] By using the Wiedemann-Franz law, the electronic thermal conductivity was determined to be less than 1.1 $Wm^{-1}K^{-1}$.

[11] M. A. Moram, Z. H. Barber, C. J. Humphreys. *Thin Sol. Films*, **2008**, 516, 8569.

[12] K. Suzuki, H. Morita, T. Kaneko, H. Yoshida, H. Fujimori, *J. Alloys Compd*. **1993**, *201*, 11; K. Suzuki, T. Kaneko, H. Yoshida, H. Morita, H. Fujimori. *J. Alloys Compd*. **1995**, *224*, 232.

[13] A. Herwadkar, W. R. L. Lambrecht, *Phys. Rev. B*. **2009**, *79*, 035126; A. S. Botana, F. Tran, V. Pardo, D. Baldomir, P. Blaha, *Phys. Rev. B*. **2012**, 85, 235118; L. Zhou, F. Körmann, D.d Holec, M. Bartosik, B. Grabowski, J. Neugebauer, P. H. Mayrhofer, *Phys. Rev. B*. **2014**, *90*, 184102.

[14] A. Togo, F. Oba, I. Tanaka, *Phys. Rev. B*. **2008,** *78*, 134106.

[15] Kresse, G. Furthmüller, J. Comput. Mat. Sci. 1996, 6, 15.

[16] P. V. Burmistrova, J. Maassen, T. Favaloro, B. Saha, S. Salamat, Y. R. Koh, M. S. Lundstrom, A. Shakouri, T. D. Sands, *J. Appl. Phys*. **2013**, *113*, 153704.

[17] M. Jonson, G. D. Mahan, *Phys. Rev.* **1980**, *21*, 4223.

[18] F. Rivadulla, M. Bañobre-López, C. X. Quintela, A. Piñeiro, V. Pardo, D. Baldomir, M. A. López-Quintela, J. Rivas, C. A. Ramos, H. Salva, J-S. Zhou, J. B. Goodenough, Nat. Mater. 2009, 8, 947; P. A. Bhobe, A. Chainani, M. Taguchi, T. Takeuchi, R. Eguchi, M. Matsunami, K. Ishizaka, Y. Takata, M. Oura, Y. Senba, H. Ohashi, Y. Nishino, M. Yabashi, K. Tamasaku, T. Ishikawa, K. Takenaka, H. Takagi, S. Shin, *Phys. Rev. Lett*. **2010**, *104*, 236404.

[19] X. Y. Zhang, J. S. Chawla, B. M. Howe, D. Gall, *Phys. Rev. B*. **2011**, 83, 165205.

[20] S. Kerdsongpanya, N. van Nong, N. Pryds, A. Zukauskaite, J. Jensen, J. Birch, J. Lu, L. Hultman, G. Wingqvist, P. Eklund, *Appl. Phys. Lett*. **2011**, *99*, 232113.

[21] H. Takiguchi, A. Matoba, K. Sasaki, Y. Okamoto, H. Miyazaki, J. Morimoto. *Mater. Trans*. **2010**, *51*, 878.

[22] H. L Gao, T. J. Zhu, H. Wang, Z. F. Ren, X. B. Zhao, *J. Phys. D: Appl. Phys*. **2012**, *45*, 185303.

[23] J. P. Heremans, V. Jovovic, E. S. Toberer, A. Saramat, K. Kurosaki, A. Charoenphakdee, S. Yamanaka, G. J. Snyder, *Science* **2008**, *321*, 554; T. M. Tritt and M. A. Subramanian, *MRS Bulletin*, **2006**, *31*, 188.

[24] A. J. Schmidt, X. Chen, and G. Chen, *Rev. Sci. Instrum***. 2008**, *79*, 114902.

[25] P. Giannozzi, S. de Gironcoli, P. Pavone, S. Baroni, *Phys. Rev. B*, **1999**, *43*, 7231.

Figures

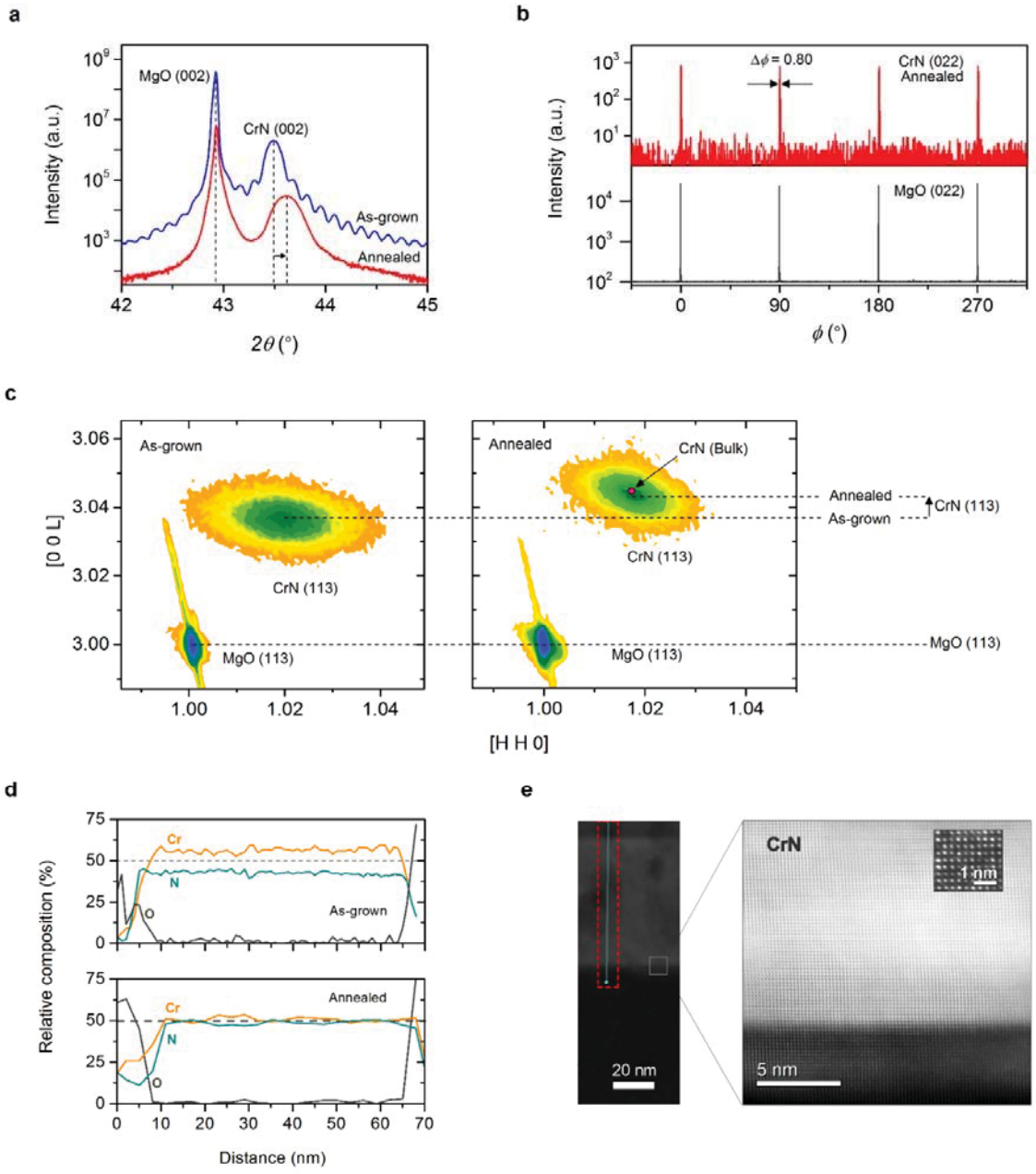

Figure 1. Structural and compositional characterization. (a) Out-of-plane θ-2 θ scan around the (002) peak of the as-grown and annealed CrN films. (b) ϕ-scan around the (022) peak of the annealed film. (c) Reciprocal space map around the (113) peak of the as-grown and annealed CrN films. (d) Relative composition derived from an EELS analysis along cross-section lamellae for both as-grown and annealed films. (e) Low-magnification STEM image of an annealed CrN film (left) with a line showing the path of the EELS analysis in panel (d). Microstructure of the interface between CrN and MgO (right) with a high-resolution STEM image in the inset.

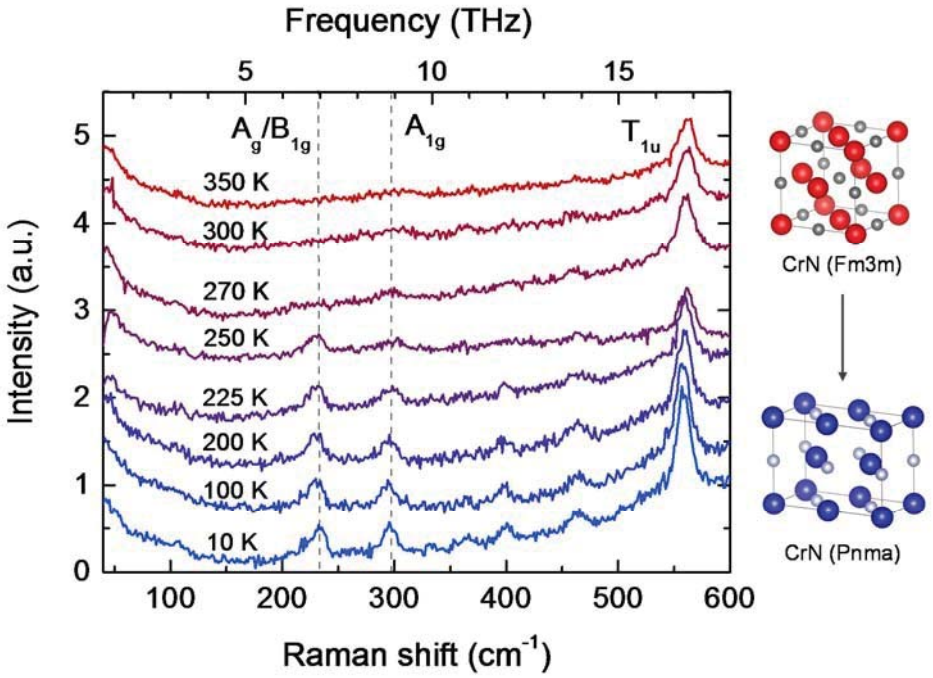

Figure 2. Temperature evolution of the Raman spectra for the annealed film. The change of some modes confirms the phase transition from high temperature rock-salt CrN, space group Fm3m, to low temperature orthorhombic CrN, space group Pnma. (Details about mode's assignments are provided in the Supporting Information)

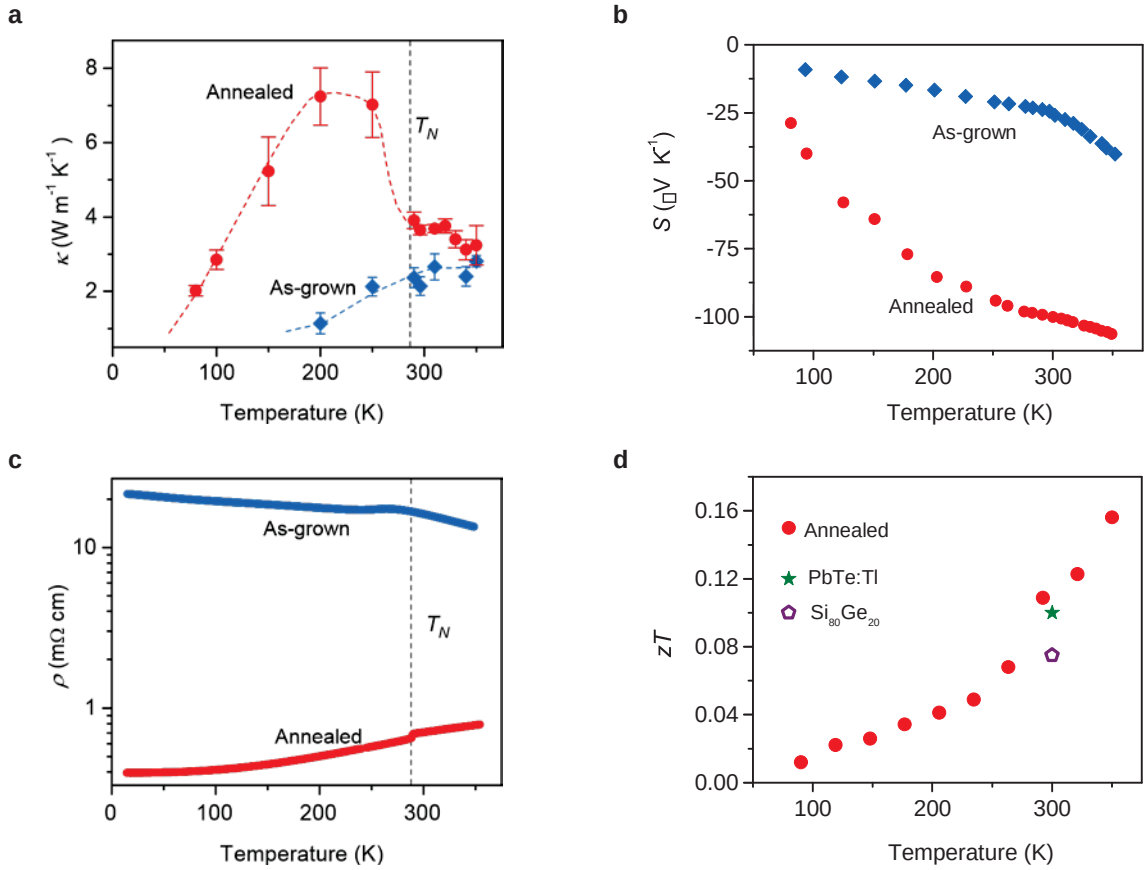

Figure 3. Thermoelectric properties for both as-grown and annealed CrN thin films. (a) Temperature dependence of the electrical resistivity, (b) Seebeck coefficient, (c) thermal conductivity, and (d) dimensionless figure-of-merit *zT*. The dotted line in (a) and (c) marks the transition between the low temperature orthorhombic phase and the high temperature rock-salt. T_N refers to the structural transition temperature. (PbTe:Tl and $Si_{80}Ge_{20}$ taken from reference 23)

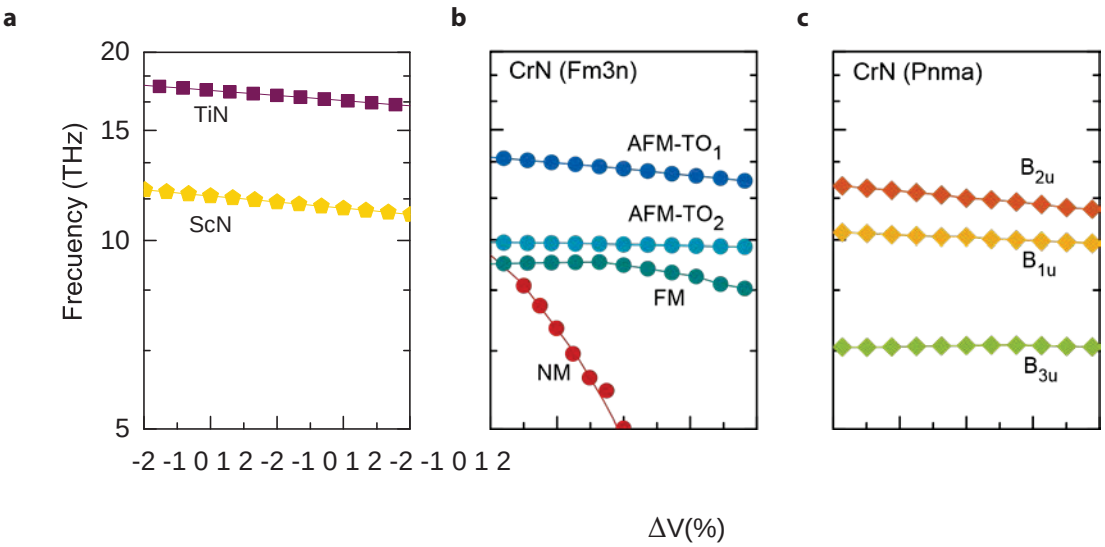

Figure 4. Calculated volume dependence of the TO phonon mode at the center of the Brillouin zone for (a) ScN and TiN, (b) rock-salt (*Fm3m*) CrN and (c) Orthorhombic (*Pnma*) CrN. In the antiferromagnetic (AFM) configuration, the TO mode splits into two degenerate modes ($AFMTO_1$ and $AFM\text{-}TO_2$) in CrN and a non-degenerate mode in non-magnetic (NM) and ferromagnetic (FM) CrN.

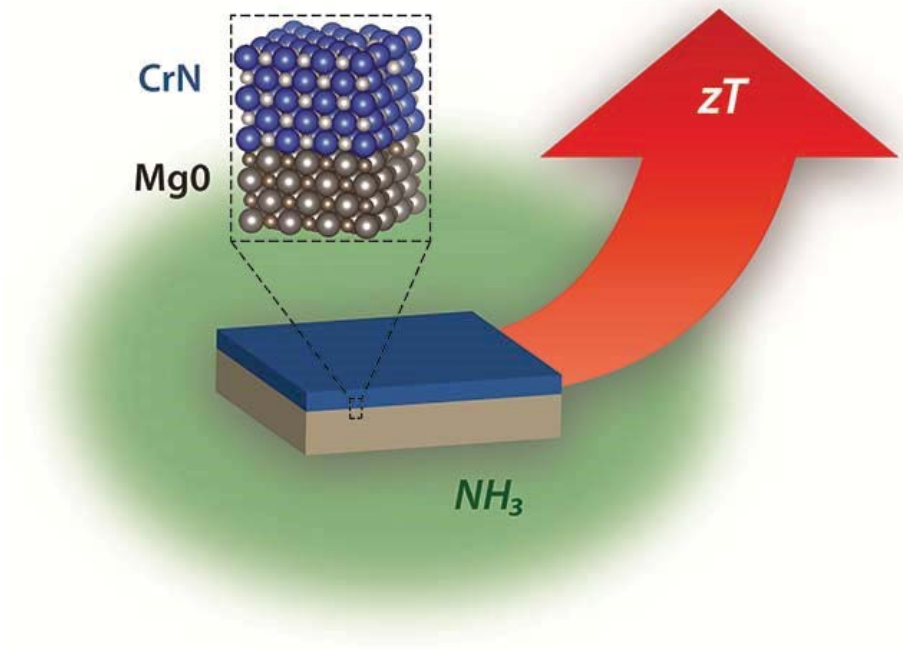

ToC Figure (55 mm broad × 50 mm high)

Supporting Information

I. Phonon mode softening and Mode Gruneisen parameter

In the *Pnma* orthorhombic cell there are 24 phonon modes (corresponding to 8 atoms each with three degrees of freedom) that can be categorized according to their irreducible reorientations. These include $4A_g$, $2B_{1g}$, $4B_{2g}$ and $2B_{3g}$ Raman active modes, $4B_{1u}$, $2B_{2u}$ and $4B_{3u}$ infrared active modes, and $2A_u$ silent modes (See **Table S1**). Similarly, in the *Pm-3m* rock-salt unit cell there are 6 phonons modes: three degenerate acoustic modes of zero frequency and three degenerate transverse optical modes, which both have T_{1u} symmetry. When the symmetry is lowered from rock-salt *Fm-3m*, (point group O_h) to *Pnma* (point group D_{2h}), the T_{1u} mode splits into B_{1u}, B_{2u} and B_{3u} modes.

As shown in Figure 5, the volume dependence of phonons for the *Pnma* phase is linear, which is similar to other early TMN, such as TiN and ScN. The volume dependence of all other modes is also linear (**Figure S1**). The calculated mode Gruneisen parameter ($\gamma = -\partial ln\omega/\partial lnV$, where ω is the mode frequency and V is unit cell volume) is similar to that in TiN and ScN. Therefore, transverse optical (TO) phonon modes in the *Pnma* phase are quasi-harmonic, which is similar to that in other early TMN. On the other hand, phonons in cubic rock-salt CrN are softer and anharmonic: the volume dependence is quadratic. As a result, the calculated mode Gruneisen parameter of rock-salt CrN is larger than that of ScN and TiN (See **Table S1**). In line with the softer phonons, the dielectric constant and the Born effective charges of CrN are very high.

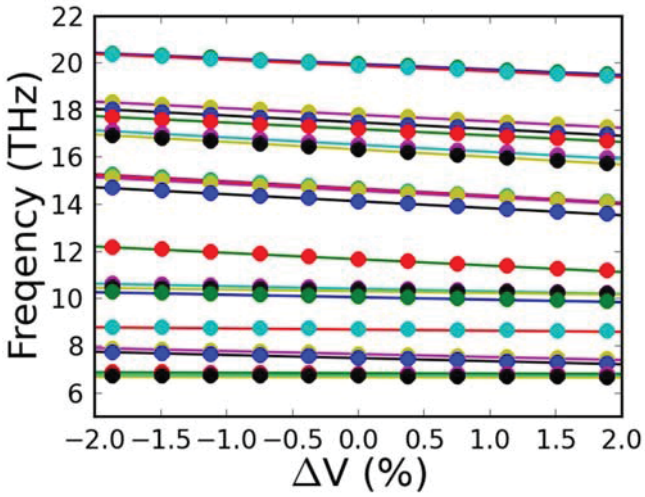

Figure S2. Volume dependence of optical phonons of *Pnma* CrN at the center of the Brillouin zone (Γ point). The circle represents the data and the line is linear fit. Different color represent different frequencies.

Compound	**Expt. Lattice constant**	**Mode Gruneisen parameter**	**Born effective charge**		**Dielectric constant**
			TM	N	
ScN	4.5[1]	2.2	3.93	-3.93	31 (total)
TiN (AFM)	4.19,[2] 4.26[3] (4.23)[4]	1.9 1.9	2.19	-1.41	2.37(Ionic)
CrN(FM)-Cubic	4.14[5]	4.1	6.46	-6.48	164 (total)
CrN(AFM)-Cubic	4.14	2.2 0.7	6.46	-6.48	165 (total)
CrN(NM)-Cubic	4.14	12	-0.60	0.99	85(total)
CrN(AFM)*Pnma*	a=5.757 b=2.964 c=4.13	1.36 (average) 2.32 (highest) 0.1 (min)	4.31	4.33	48(*xx*) 41(*yy*) 38(*zz*)

Table S1. Mode Gruneisen parameter of cubic CrN compared with its orthorhombic *Pnma* phase and other early transition metal nitrides

TO phonons in the cubic phase can be lower than that in the orthorhombic cell. It is known that high temperature phase rock-salt CrN is paramagnetic (PM). The random fluctuation of local moments creates a large number of magnetic configurations, and each configuration has its own unique phonon spectra. As a result, each mode has a distribution of frequencies with the lowest value corresponding to non-magnetic (NM) configurations and the highest to AFM configurations. The latter and former are the lowest and highest energy configuration, respectively, with the latter being magnetically closer to the AFM configuration of the orthorhombic cell. As shown in Figure 1 (b) and (c), at the center of the Brillouin zone B_{1u} and B_{2u} the modes have a similar frequency to that of the AFM cubic phase. The B_{3u} mode in the *Pnma* phase is lower in energy compared with the other modes; however, the cubic CrN shows a sign of instability at the zone boundary (see phonon band diagrams for different phases in **Figure S2**). In the FM phase, instability appears at the X points. The NM phase shows instability at several points in the Brillouin zone. These unstable phonon modes are clearly softer in CrN depending upon the magnetic configuration of the stable phonon modes in the *Pnma* phase.

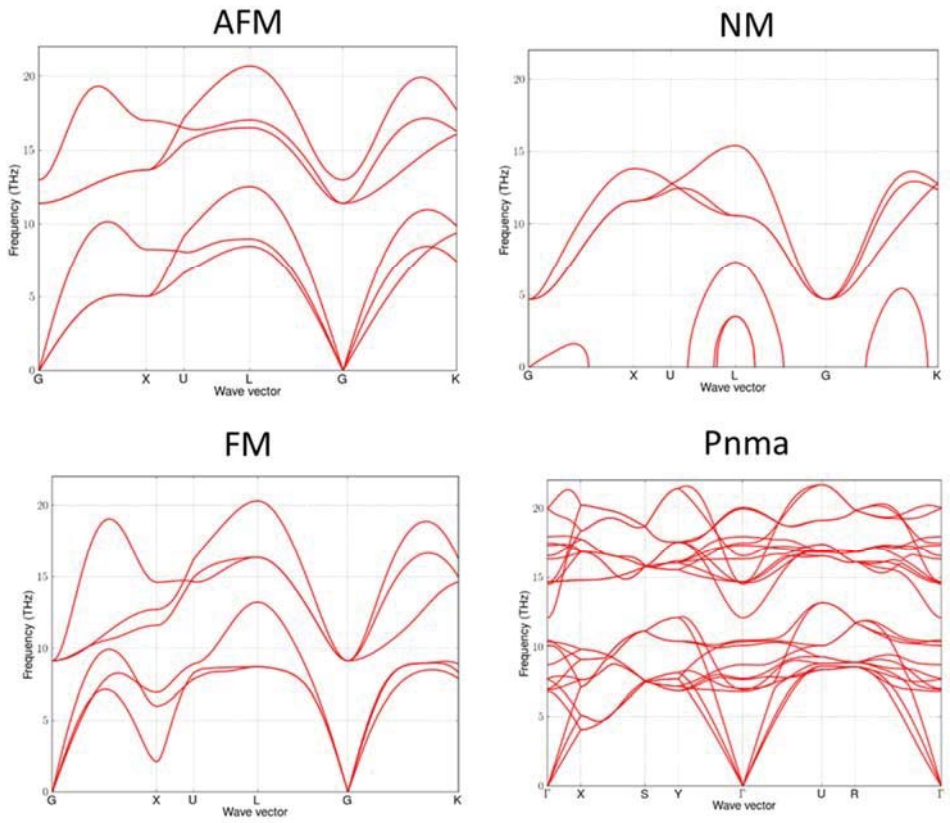

Figure S2. Phonon band structure of the cubic (in different magnetic configurations) and the orthorhombic (*Pnma*) phase of CrN. The phonon spectra were calculated at an experimental lattice constant in PBE+U approximation with U = 3.0 eV for Cr 3*d*-orbitals.

II: Raman Spectra and Phase Transitions

In back scattering geometry, the direction of incident (k_i) and scattered light (k_o) are parallel and their polarizations (e) are perpendicular to the ***c*** axis of the crystal. As a result, we are only concerned with modes whose Raman tensor has non-vanishing elements along the *xx, yy*, and *xy* directions. In Table S2, which lists the Raman tensor for all of the active modes, it can be observed that the A_{1g} and B_{1g} modes are activated. In Figure 3, the corresponding calculated modes to the peak in the orthorhombic and rock salt phase are labelled. Clearly, the main peak around 16.3 THz (556 cm^{-1}) corresponds to either the fourth A_g peak or the second B_{1g} peaks, or one of them if other intensity is small. The first peak can be attributed to the first A_g mode at 7.0 THz (232 cm^{-1}), the first B_{1g} mode at 6.9 THz (233 THz), or a combination of both. The second peak at 8.7 THz corresponds to the A_{1g} peak at cm^{-1}. The calculated phonon mode at 14.6 either has a small Raman intensity or creates a small shoulder to the main peak and it is hard to discern experimentally.

Ag	B1g	B2g	B3g	A_u	B1u	B2u	B3u
x^2 y^2 z^2	*xy, Jz*	*xz Jy*	*yz Jz*	-	*z*	*y*	*x*
7.015 **(6.97)**	6.917**(6.97)**	10.358	7.645	7.735	0	0	0
8.716 **(8.86)**	16.582 **(16.7)**	10.483	17.940	17.308	10.110	14.513	6.793
14.639		17.477			14.680		12.097
16.338**(16.7)**		20.050			19.956		14.686

Table S2. Irreducible representation of phonons in orthorhombic (*Pnma*) CrN. The corresponding experimental values are shown in brackets.

***Pnma*(D_{2h})**	**Ag**			**B1g**			**B2g**			**B3g**		
	x	y	z	x	Y	z	x	y	z	x	y	z
x	*a*	.	.	.	*D*	.	.	.	*e*	.	.	.
y	.	*b*	.	*d*	.	.	.	.	.	.	.	*f*
z	.	.	*c*	.	.	.	*e*	.	.	.	*f*	.

Table S3. Raman tensor of phonon modes of different irreducible representations. a, b, c, d, e, and f correspond to a non-zero Raman intensity.

When the temperature increases beyond 286 K, all peaks disappears except the main peak at 16.3THz. This is due to the change of symmetry during the phase transition from a structure without inversion symmetry to a structure with inversion symmetry. The Raman tensor is the second ranked symmetric tensor and hence vanishes in the cubic rock-salt crystals; however, the disorder present in the sample could break the symmetry locally and allow for the first order Raman process. The source of the disorder could be magnetic or could be a defect such as nitrogen vacancy in crystals. Due to the fact that the momentum conservation requirement relaxes in the disorder-induced Raman spectra, they roughly corresponds with the weighed phonon density of states. As seen from the phonon density of state (**Figure S4**), There is a peak at ~16.3 THz, which corresponds to the TO bands at the L points.

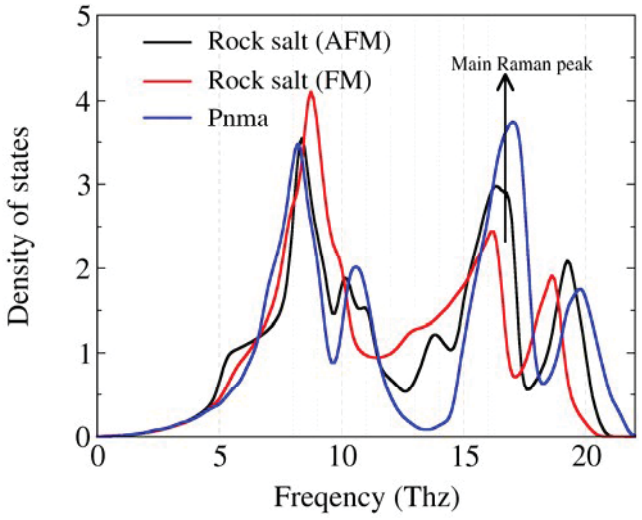

Figure S4. Phonon density of states of rock-salt CrN in the AFM phase compared to that of the orthorhombic (*Pnma*) phase. AFM has the lowest energy of FM and NM magnetic configurations.

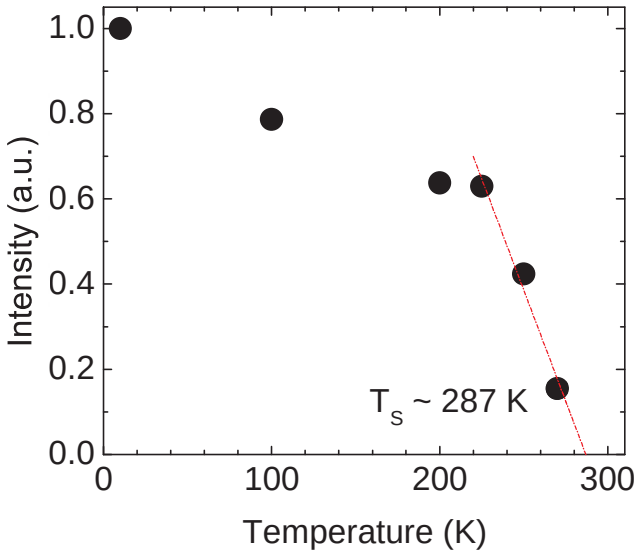

Figure S5. Temperature dependence of the 7 THz Raman mode for the annealed sample.

III: Carrier Mobility

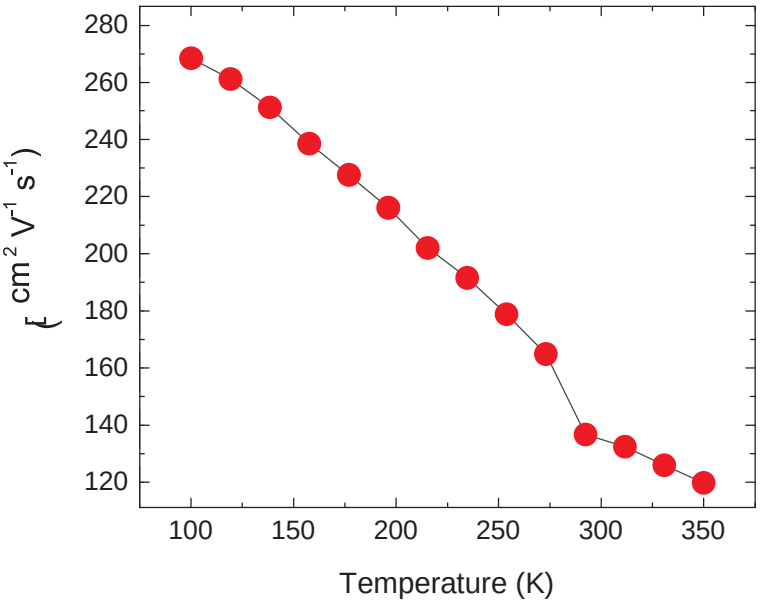

Figure S6. Temperature dependence of carrier mobility for the annealed sample.

References for the Supporting Information.

[1] W. Lengauer, *J. Solid State Chem.* **1988**, *76*, 412.
[2] S. Nagakura, T. Kusunoki, F. Kakimoto, Y. Hirotsu, *J. Appl. Crystallogr.* **1975**, *8*, 65.
[3] *JCPDS* **n.d.**, *38-1420*.
[4] P.R. LeClair, *Titanium Nitride Thin Films by the Electron Shower Process*, Massachusetts Institute of Technology, **1998**.
[5] J. Hastings, L. Corliss, *Phys. Rev.* **1962**, *126*, 556.